JOURNAL OF MATERIALS SCIENCE 33 (1998) 3839–3848

Surface quality and laser-damage behaviour of chemo-mechanically polished CaF_2 single crystals characterized by scanning electron microscopy

H. JOHANSEN, G. KÄSTNER
Max-Planck-Institut für Mikrostrukturphysik Halle, Weinberg 2, 06120 Halle, Germany
E-mail: johansen@mpi-halle.de

A significant increase in the ultraviolet laser-damage threshold of CaF_2 (1 1 1) single-crystal surfaces after surface finishing by chemomechanical polishing (CMP) with colloidal silica has been demonstrated as compared to conventional mechanical-abrasive polishing (MAP). It was shown that CMP yields an up to 12-fold increase of the damage threshold fluence up to $F_{th} = 30\,J\,cm^{-2}$ for 1-on-1 nanosecond pulses of 248 and 193 nm excimer laser irradiation. Even after 5-on-1 irradiations, the damage threshold remains as high as $F_{th} = 15\,J\,cm^{-2}$ in the case of CMP. For both polishing procedures, the change in dielectric surface properties has been characterized by means of scanning electron microscopy (SEM) using electron beam-induced charge-up phenomena. These were mainly detected by the variation of emitted secondary electron (SE) yield δ_{SE} depending on the primary electron (PE) energy. Two kinds of charge-up phenomena were employed: (i) the onset or vanishing of statistically fluctuating SE yield bursts during slow-scan imaging (''stripe pattern'' method), and (ii) the temporal decay of the electron beam-induced charge-up inside an electrically conducting mask (charge decay method). Both these phenomena disappeared after CMP. It is concluded that this disappearance results from removing the subsurface damage layer which is typical of MAP. © *1998 Kluwer Academic Publishers*

1. Introduction

Today, ultraviolet and near X-ray optics are favoured for lithographically structuring photoresists below 0.25 nm [1]. Owing to the high intensity of light necessary for a large throughput, low optical losses are required. While bulk losses have indeed been reduced considerably, the lowering of surface losses remains a challenge. The scattered light per single surface of a CaF_2 lens has to be less than 0.5%, and the laser damage resistivity of a complete optical system has to be of the order of 10^{10}–10^{11} pulses in the $0.1\,mJ\,cm^{-2}$ range. Submicrometre-sized absorbing particles located in dielectrics give rise to local inclusion heating to a few thousand degrees Kelvin [2]. Consequently, the realization of high-grade optical surfaces is closely accompanied by the development of adequate methods of failure analysis of the manufactured surfaces [1–5].

In principle, mechanical abrasive polishing (MAP) results in sufficiently flat surfaces, but their subsurface layer is known to be damaged, i.e. strongly disturbed on an atomic scale. It is known that this damage layer can be removed by subsequent Chemo-mechanical polishing (CMP) [6, 7]. In particular, CMP finishing of optical surfaces reduces anisotropy produced during any preceding MAP treatment [8] and avoids the generation of dislocations [9]. Today, the transfer of commercial semiconductor CMP technologies [10] to optical materials is under way [11].

To determine the microtopography of polished surfaces down to about 0.1 nm, profilometric techniques (e.g. mechanically contacting nanostep profilers or contactless optical heterodyne profilers [12, 13]) as well as atomic force microscopy [14], are used. Additional information can be obtained from measuring the integrated scattered light [15] or from surface acoustic waves [16]).

Information to be deduced from further properties – including the electrical charging behaviour of surface-near states – can be obtained by means of SEM as will be explained in more detail. The secondary electron (SE) yield of insulators remarkably depends on the surface microroughness [17]. This results in specific charge-up processes, depending on the primary charge injection mechanism at a chosen primary electron (PE) energy [18, 19]. This charge-up behaviour changes drastically if the subsurface damage layer produced by MAP is removed. This causes a decrease in the concentration of surface-near defects [20, 21]. However, MAP or CMP finishing of dielectric surfaces cannot solely be characterized in terms of surface topography (e.g. scratches, microcracks, grain size, pores, etc.). In addition, the most instructive scanning probe methods reveal the local and overall charge-up of an insulator surface. This holds, particularly, for MAP-treated dielectrics because, according to our experience, the microtexture of defective top layers [22] cannot be identified by the usual SEM crystal

orientation mapping [23]. On the other hand, transmission electron microscopy (TEM) of cross-sections can determine whether damage is present [24] or not [25].

The present paper will show that the properties of surfaces of dielectrics treated by MAP and CMP can be characterized by the dependence of SE yield on the local electron beam-induced charge-up. As an example, for the case of insulating materials, experiments were carried out on (1 1 1) oriented surfaces of CaF_2 single crystals. The improved surface properties of CMP-treated surfaces compared to MAP will be correlated with the essentially improved ultraviolet laser damage threshold.

2. Experimental procedure

(1 1 1)-oriented surfaces of CaF_2 single crystals were mechanically polished with 0.25 μm diamond suspension. Subsequent CMP was performed with colloidal silica under constant pH on a commercial polishing machine. In addition to SEM, to study microtopography in a sensitive way, deep etching was performed in 0.2 N HNO_3 solution for 15 min at room temperature. TEM of cross-sections was carried out to estimate the thickness of the subsurface damage layer after MAP.

Laser damage tests were performed by 1-on-1 and N-on-1 irradiation pulses in air for 248 nm/14 ns and 193 nm/8 ns pulses in the fluence range $1\,J\,cm^{-2} < F < 40\,J\,cm^{-2}$. Subsequently, the surfaces were prepared for SEM investigations in two different ways: (i) the cleaned uncovered crystals were electrically grounded through eight peripheral carbon conducting dots in order to employ the stripe-pattern charge-up method described in Section 3.1; (ii) an aluminium grid mask 0.5 μm thick was evaporated (in two steps through a slit mask turned 90° after the first step) to produce meshes $1.5 \times 1.5\,mm^2$ in size separated by aluminium bars of 0.5 mm width. These masks were grounded at their periphery by carbon conducting dots in order to employ the charge decay method described in Section 3.2.

SEM studies were performed in a field-emission gun microscope at primary electron energies of $0.5\,KeV \leqslant E_p \leqslant 10\,keV$. Specimen tilting up to $\Phi = 50°$ was applied. Before taking slow scan micrographs, the distribution of electron beam-induced charge-up was stored in an image memory device. All SE contrast images shown below correspond to *reproducibly* generated charge distributions on the crystal surface. Very small laser-induced surface modifications yield a pronounced capacitive component during SE imaging. Thus they can only be detected by using a very short dwell time of the electron probe (TV scan mode) under high specimen tilting.

3. Fundamentals of electron beam-induced charging of insulators during SEM observations of defective surface layers

The electron beam-induced surface potential of an insulator is determined by the energy and the intensity of the PE, the dwell time of the electron probe, and the SE yield of the material. (The dwell time, which is of the order of microseconds in the slow scan mode, is defined by the line time divided by the number of pixels per line.) The SE yield itself is influenced by the surface properties of the material in a complicated way (e.g. by microroughness, band structure, mean free path length, energy loss per unit length, and depth of emission of the SE [17, 26, 27]).

In general, a clean insulator surface can charge either positively or negatively under electron irradiation, depending on the energy, E_p, of the primary electrons. A positive surface potential which results from a *total* electron yield $\sigma = \delta + \eta > 1$ (δ = SE yield, η = backscattering coefficient) usually occurs within an interval $E_1 < E_p < E_2$ while it is negative outside this interval. This E_1–E_2 interval is far greater in insulators than in metals. For both the critical energies E_1 and E_2, the total yield is $\sigma = 1$. However, charging in the SE mode is also a function of the incident angle of the PE, i.e. the tilt angle, Φ, between the electron beam and the surface normal of the specimen. The SE yield, δ, is known [28] as

$$\delta(E_p, \Phi) = (BE_p\lambda)/(e_i R_e \cos\Phi) \times \{1 - \exp[-(R_e/\lambda)\cos\Phi]\} \qquad (1)$$

where λ is the escape depth of SE, B is a constant less than unity, e_i is the average energy to produce a single SE, and R_e is the electron range. The nearly inverse proportionality between δ and $\cos\Phi$ is well known: an increasing tilt, Φ, enhances the positive charge-up if $E_p < E_2$. If $E_p > E_2$ increasing tilt compensates the negative charge-up towards a surface free of charge [19].

It should be noted that in the case of a positive charge-up at $E_p < E_2$ a more complicated behaviour results: the insulator's positive surface layer can partly be neutralized because it attracts the SE electrons, both from outside and inside the material [29]. In this way, the positive surface layer becomes "sandwiched" between two negatively charged layers. Both of them reduce the SE emission probability. Contrary, for $E_p > E_2$ and $\sigma < 1$ the negative surface potential extends into a much greater depth, d_b (in spite of a positively charged surface layer only few nanometres thick which also exists in this case). Hence, d_b controls the emission of the SE into the vacuum. Accordingly, the SEM charging phenomena for $\sigma < 1$ and $\sigma > 1$ are very different and they are defined by the size of the excitation volume of the PE. Both models suppose dynamic equilibrium during the scanning electron beam irradiation. If this equilibrium is modified by the local presence of defects, the resulting charge-up mechanisms vary locally, resulting in some kind of defect imaging. In particular, a sensitive characterization of the surface properties of dielectrics is enabled by the two different SEM techniques mentioned above.

3.1. Electron beam-induced positive charge-up processes in the energy range $E_1 < E_p < E_2$

In this case, the charged triple layer (negative, positive, negative) reduces the escape depth of the SE, so that

bulk charge influences can be mainly excluded. Therefore, a contrast due to a reduced SE emission (i.e. loss of information) and arising only from a small excitation volume can be expected. If the material has a dielectric time constant $\tau = \rho \cdot \varepsilon$ (ρ = electrical resistivity, ε = dielectric constant) in the order of the line time, t_1, for slow scanning ($\approx 10^{-2}$ s), SE yield changes due to defects should mainly appear within a single scanning line. In CaF_2, however, the time constant is $\tau \approx 7$ s (compared, for example, with 400 s for quartz and 10^{-20} s for copper [30]). Hence, $\tau \gg t_1$, i.e. sudden changes of charge rarely occur inside a single scanning line. They rather occur during a time which comprises *groups* of lines, thus leading to "stripe pattern". This pattern indicates fluctuating charge phenomena, i.e. changes of the effective charge density on the insulator surface. These fluctuations can be quantitatively processed by pulse height analysis [31].

An example is shown in Fig. 1 for a MAP-treated CaF_2 (1 1 1) surface containing a local inclusion. The stripe pattern is observed at specimen inclination of $\Phi = 32^\circ$ as shown in Fig. 1a. This pattern is observed to be independent of the specimen size and the size of the scanned area. At normal incidence of the electron beam, the stripes nearly disappear, as shown in Fig. 1b. Here, E_p and Φ were chosen to work below the critical limit of charge-up (cf. Section 4.1).

CaF_2 is an excellent ionic conductor [32] and its electronic conductivity of $\rho \approx 10^{-13}\,\Omega^{-1}\mathrm{cm}^{-1}$ reported for vacuum-deposited CaF_2 films [33] is remarkably higher in comparison to 10^{-17}–$10^{-20}\,\Omega^{-1}\mathrm{cm}^{-1}$ for polymers, mica or PTFE [34]. Therefore, it can be expected that the dynamic equilibrium between charging and discharging of the CaF_2 surface under low-energy electron irradiation is shifted towards discharging, for MAP- as well as for CMP-treated surfaces.

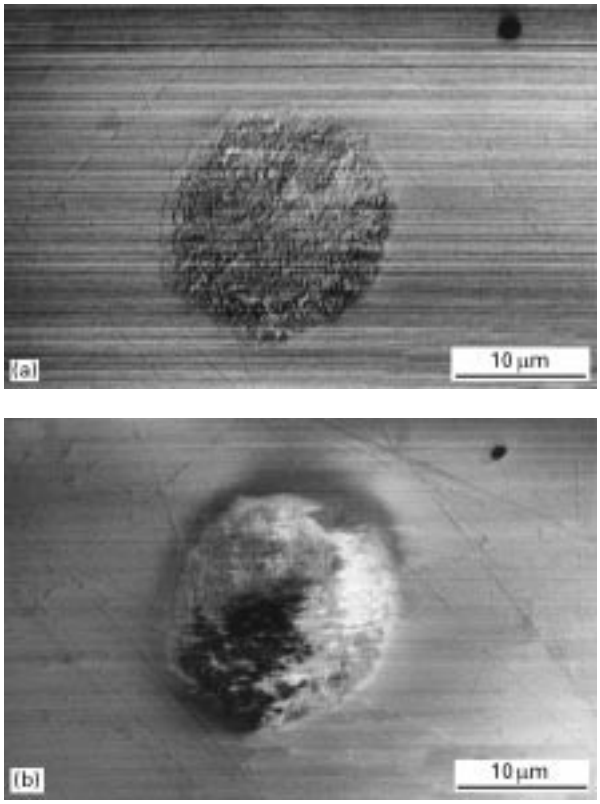

Figure 1 Charge-up behaviour during 2 kV SEM imaging of a MAP-treated (111) surface of CaF_2 (a) Tilting to $\Phi = 32^\circ$ generates a stripe pattern typical of positive charge-up. (b) A surface nearly free of charge at $\Phi = 0^\circ$. Note also the change in contrast of the inclusion.

3.2. Localized charge decay after negative charge-up at $E_p > E_2$

Whereas positive charge-up behaves independently of the specimen size (charge-up can equally well arise from outside the scanned area), the *decay* behaviour of negative charge should be studied within well-defined, subdivided areas of the insulator surface, each surrounded by a grounded conducting path. Experimentally, this subdivision has been accomplished by evaporating a conducting aluminium mesh as explained above. The imaging procedure consists of two steps. First, all mesh areas are *uniformly* charged up negatively by a beam energy $E_p > E_2$. Then, the voltage is reduced to $E_p < E_2$ in order to slow down the charge decay and to get nearly maximum SE yield. This decay is found to behave differently in various meshes, thus indicating different concentrations of effective electron traps. In order reliably to compare this charge decay within different meshes, the leakage paths to nearby existing grounded contacts must have the same length. Otherwise, uncontrolled blurring starting from anywhere on the insulator surface prevents localization of the different concentrations of traps.

This charge decay method is demonstrated in Fig. 2. An imperfect CaF_2 (1 1 1) surface is imaged at $E_p = 0.9$ keV after preceding charge-up at $E_p = 5$ keV. Inside the grounded aluminium meshes, local- and time-dependent features of intensity are seen which indicate charge leakage to ground that behaves differently from mesh to mesh. These differences can be interpreted as "decoration patterns" arising from locally *different* concentrations of surface defects.

In the case of dielectrics, the electron range, R_e, of the PE is, fortunately, nearly as large as the average depth of the centre of the total charge induced by the electron probe [34]. Moreover, both quantities are comparable to the thickness of the subsurface

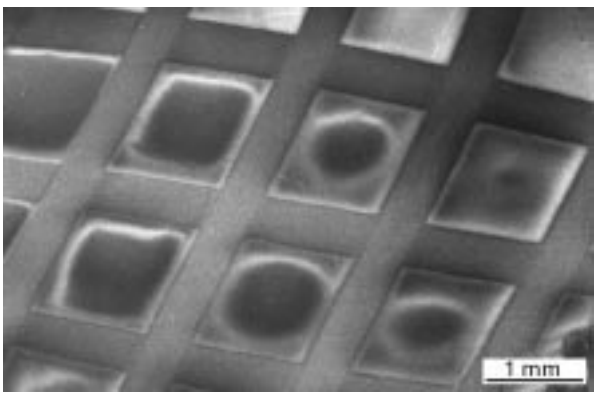

Figure 2 Charge decay behaviour of a MAP-treated (111) surface of CaF_2 SEM imaging at $E_p = 0.9$ keV, $\Phi = 0^\circ$ of different charge decay features inside the meshes of a grounded aluminium cross-grid, starting from a preceding negative charge-up at $E_p = 5$ keV.

damage layer produced by MAP. A typical figure is $R_e = 0.3\,\mu m$ in CaF_2 at $E_p = 5\,keV$ [35].

A further favourable fact is the large mean free path of SE in insulators which leads to a high probability that SE generated at a depth R_e can reach the surface [26]. Therefore, a sufficient SE emission from the insulator surface is observed, although the ionization energy, e_i, to generate a secondary electron is very high ($e_i \approx 2.8\,E_g$ in dielectrics where E_g is the band gap energy, e.g. $E_g\,(CaF_2) = 12.1\,eV$ [17]).

4. Results

4.1. Charge-up of the insulator surface

The charge-up behaviour of the CaF_2 surface strongly differs for MAP and CMP treatment. The high degree of surface damage produced by MAP is seen in Fig. 3 where most of the polishing scratches are visible without tilting the surface. On systematically tilting such a surface during SEM observation at a constant $E_p \approx E_2$ a critical tilt angle Φ_c, is found above which the stripe pattern appears, which results from fluctuating positive charge-up as shown in Fig. 1a. For MAP, this Φ_c was found to scatter within a narrow range of $\Delta\Phi_c = 2^\circ$. (For comparison, a beam-induced negative charge-up would lead to potential distribution patterns of total different nature [29, 36]).

After CMP, the crystal surface behaves in quite a different way, as shown in Fig. 4a and b. At a constant $E_p \approx E_2$, a very weak stripe pattern is seen which does not depend on the inclination Φ. A positive charge-up can only be reached in the energy range $E_1 < E_p < E_2$ if $\Phi > 30^\circ$ ($E_{eff} = E_p\cos^2\Phi \approx 0.5\,keV$ [19, 36]). Then, the stripe pattern appears clearly, as shown in Fig. 5. However, contrary to MAP, the transition region, $\Delta\Phi_c$, is much larger for CMP.

For the surface quality achieved by CMP, a microroughness of the order of $R_a = 0.5\,nm$ (centre-line on average) is measured according to Fig. 4c. After ultrasonically cleaning CMP-treated surfaces with alcoholic solutions, the stripe patterns disappear completely if the same imaging conditions are used as in Fig. 5. Thus the positive charge-up is sensitive to weak polishing residues of CMP.

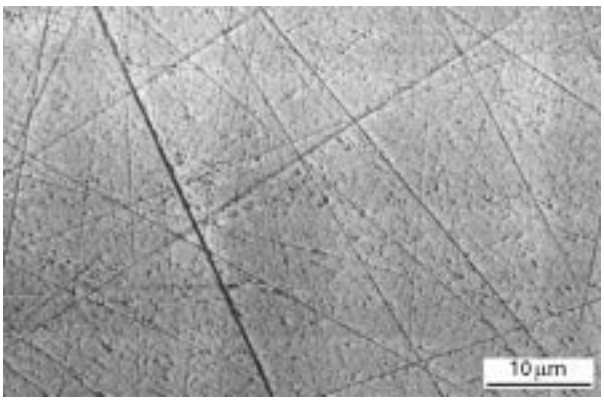

Figure 3 The (111) surface of CaF_2 MAP treated with 0.25 µm diamond. SEM imaging at $E_p = 5\,keV$, $\Phi = 0^\circ$.

4.2. Charge decay behaviour

As mentioned above, an aluminium grid was evaporated on to the surfaces in order to observe the charge decay within the individual meshes of the grid. To check whether the electrical contact of the grid is as uniform as required, possible SE yield variations were checked up to the periphery of the crossing grid at a high magnification and in both the electron ranges

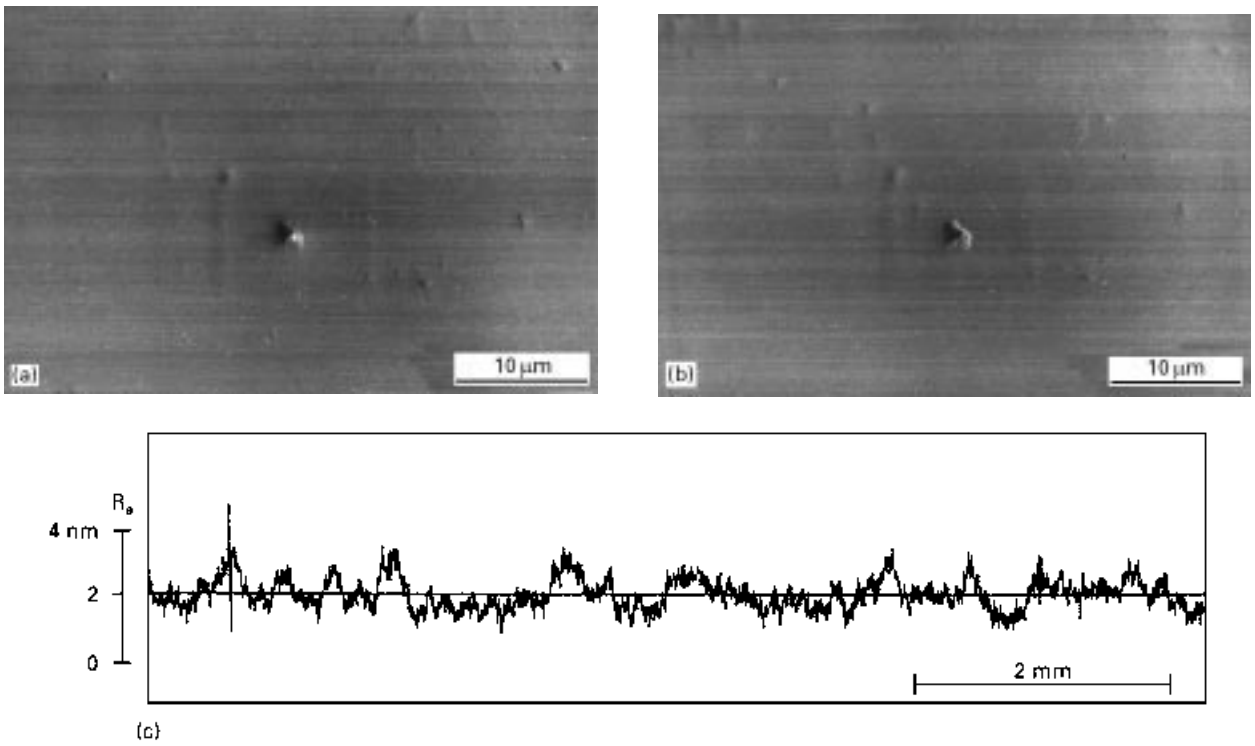

Figure 4 Charge-up behaviour of a CMP treated (111) surface of CaF_2. SEM imaging under the same conditions as in Fig. 1 ($E_p = 2\,keV$): (a) $\Phi = 0^\circ$, (b) $\Phi = 32^\circ$. The profilometer trace (c) yields a microroughness $R_a = 0.48\,nm$ (centre-line on average).

$R_e < d_{Al}$ and $R_e > d_{Al}$. Although the physical nature of the metal–insulator contact is not well known, it has been found to be constant across the whole grid.

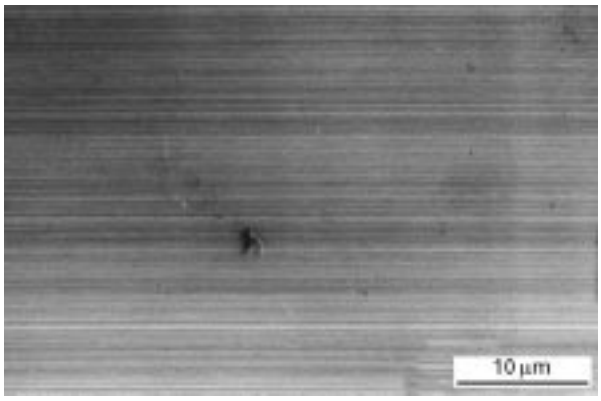

Figure 5 SEM stripe pattern of a CMP-treated (111) surface of CaF_2, indicating positive charge-up in the range $E_1 < E_p < E_2$ at $E_p = 0.9\,keV$, $\Phi = 32°$.

After an initial negative and uniform charge-up at an elevated voltage of 5 kV, the subsequent charge decay was observed at 0.9 kV within the individual meshes. This decay was found to occur slowly for MAP-treated surfaces but very rapidly in the case of CMP. The case of MAP is shown in the sequence of Fig. 6a–e. The decay first seen as a non-uniformity in the contrast starts at $E_p = 5\,keV$ after four slow scan periods of $t_f = 80\,s$, as shown in Fig. 6a. The further decay events (Fig. 6b–e) were observed within a time of 400 s at a low acceleration voltage of 0.9 kV, chosen in order to slow down the decay and to obtain maximum SE yield. The final state, Fig. 6e, reveals a total contrast inversion and a uniform positive charge inside the meshes. For intermediate states, the meshes show different charge patterns which gradually turn into the final state. The inhomogeneous charge distribution within a given mesh can be considered as a "decoration pattern". However, it is not accompanied by corresponding topographic features detectable by SE.

In the case of CMP-treated surfaces, the uniform charge-up within the meshes requires an accelerating voltage of $\geqslant 9\,kV$ as well as about three times the number of frame scans necessary for MAP to charge-up. The subsequent charge decay process observed at 0.9 kV now happens very rapidly during the first frame scan of 80 s duration, thus arriving at the final stage, as

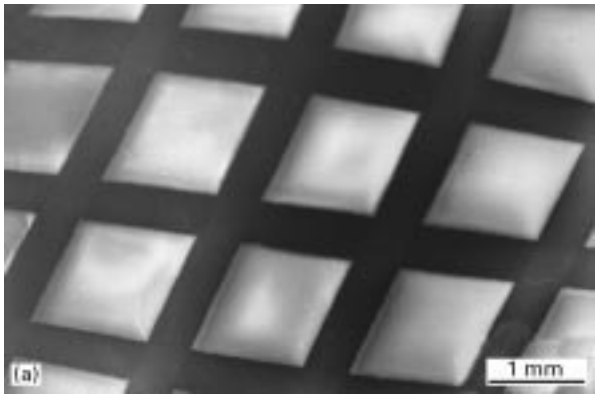

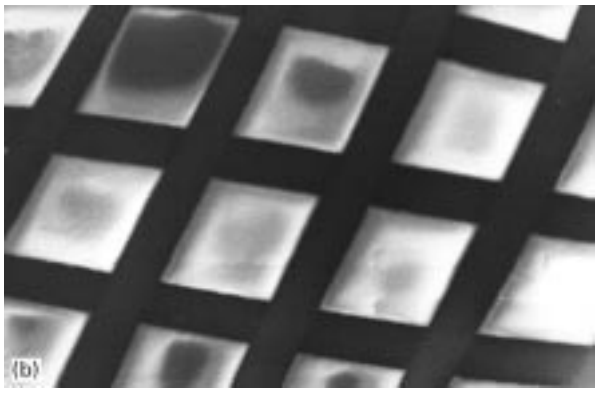

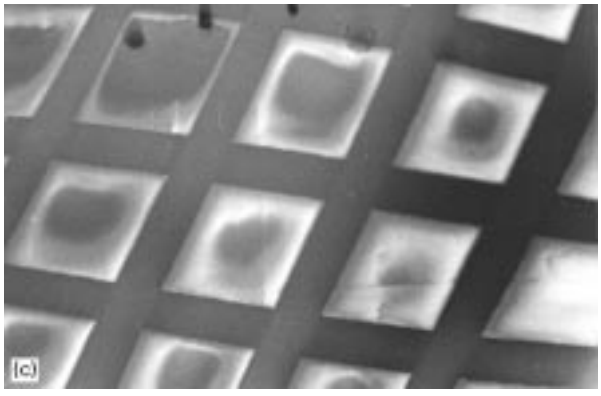

Figure 6 Successive stages of charge decay on a MAP-treated (111) surface of CaF_2 inside the meshes of an evaporated, grounded aluminium cross-grid; $\Phi = 0°$. (a) Charge-up at $E_p = 5\,keV$, (b–e) charge decay observed at $E_p = 0.9\,keV$ after (b) 160 s, (c) 240 s, (d) 320 s, and (e) final state (where a topographic feature is arrowed).

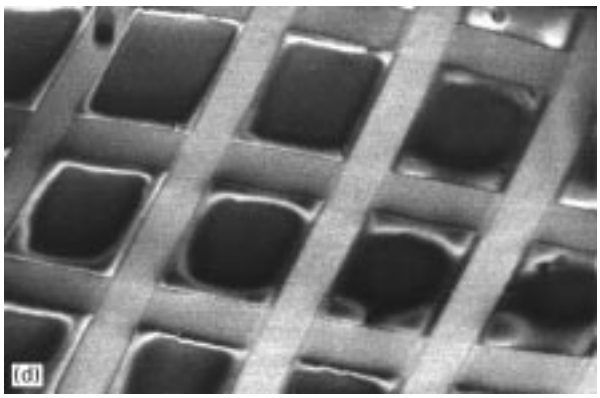

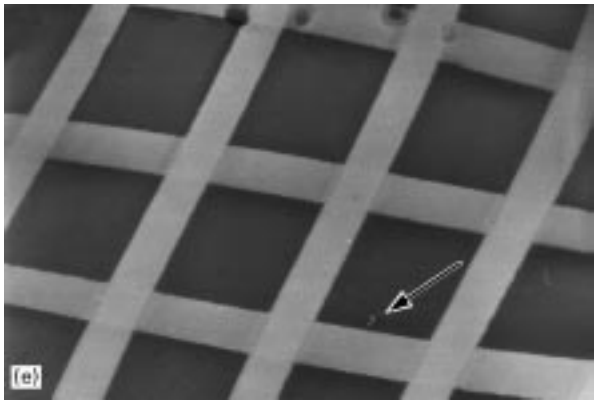

in Fig. 6e. Intermediate states or laterally non-uniform potential distributions have not been observed so far.

4.3. UV laser damage tests of MAP and CMP surfaces

As pointed out above, CMP-treated CaF_2 surfaces reveal a significantly higher laser damage resistivity than MAP-treated surfaces. In both cases, the first stages of surface damage after 1-on-1 excimer laser irradiation become visible by small SE yield differences with respect to the unirradiated surroundings. The fluence necessary to produce this effect is about 12 times higher compared to the same effect of MAP-treated surfaces.

In this latter case of MAP, first surface modifications were already found for $F = 1.7\,J\,cm^{-2}$ of 248 nm pulses. As shown in Fig. 7, three different stages of damage were observed: (I) weak interaction where polishing scratches across the laser spot still remain clearly visible (Fig. 7a); (II) pronounced charge-up of the laser spot and diminished contrast of the polishing scratches (Fig. 7b); (III) first oriented cracks inside the spot due to crystallographic chipping, accompanied by an evaporation "halo" outside the spot (Fig. 7c). In general, it should be noted that first oriented laser-induced cracks can be detected much more easily by characteristic local charge-up events during normal incidence of the electron proble for $E_p > E_2$, than by imaging topographic features free of charge (on using high specimen tilt together with SEM tilt correction). In stage II, charge-up inside the spot can be neutralized by increasing the surface tilt angle. The critical angle, Φ_c, has been observed to be sensitive to the defect density introduced by different laser fluences F, a feature shown schematically in Fig. 8a. According to Fig. 8b, increasing fluence (i.e. increasing defect *density*) requires an increasing critical tilt angle. Within such laser damage spots uncharged, scratches introduced by MAP become clearly visible.

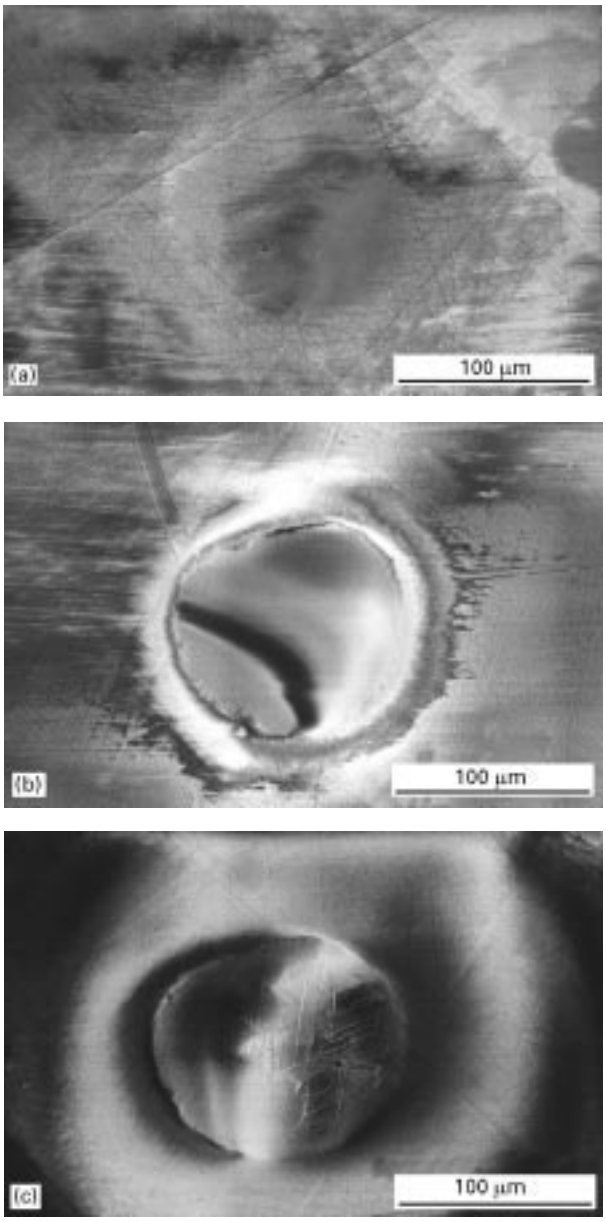

Figure 7 Single-shot 248 nm laser damage spots produced by various laser fluences, F, on CaF_2 after MAP. SEM imaging at $E_p = 5$ keV: (a) $F = 2.85\,J\,cm^{-2}$, $\Phi = 0°$, scratches are still visible; (b) $F = 9.39\,J\,cm^{-2}$, $\Phi = 27°$, charge-up inside the spot; (c) $F = 12.54\ J\,cm^{-2}$, $\Phi = 19°$, oriented microcracks inside the spot and "halo" formation outside it.

Contrary to this, after CMP, a drastically higher damage threshold has been found: even for single-shot fluences of $F > 30\,J\,cm^{-2}$ and at high specimen tilting $\Phi > 40°$ the laser spot's circular border line only could be detected (Fig. 9a, $\varnothing_\ell \approx 110\,\mu m$). The contrast of this line can be interpreted topographically as a small circular depression throughout the spot area (the SE detector position is on the right). This border line represents the site of the highest temperature gradient during irradiation, leading to the largest thermoelastic stress [37, 38]. For increased fluences, it was difficult to localize the damaged areas: only a very small increase of the SE yield could be detected by means of a very short dwell time of the electron probe under a strongly inclined specimen position (Fig. 9b). Topographic surface features could not be uniquely identified in this case. Charge-up inside the laser spots could not be found.

However, stronger laser damage of CMP-treated surfaces leads to (1 1 1)-oriented microcracking (chipping) into tiles, similar to stage III of MAP surfaces. Early stages of this topography can be observed in the SEM at high specimen tilt, as shown in Fig. 10. After a fluence of $F = 13\,J\,cm^{-2}$, $N = 5$ shots are sufficient to produce distinct *accumulated* damage structures. This kind of threshold damage becomes visible as oriented microcracks located in micrometre-sized partial damage areas of the total spot. After higher fluences of $F > 18\,J\,cm^{-2}$ a possible dependence of this threshold damage on the UV photon energy could not be stated unambiguously. Occasionally, even the threshold for 193 nm was higher than for 248 nm.

4.4. TEM of cross-sections at polished surfaces

TEM is able to reveal details of the subsurface damage layer, as is known from several crystalline materials. To obtain more evidence in the case of the CaF_2 crystals polished in this work, thin cross-sections were prepared and investigated by TEM diffraction

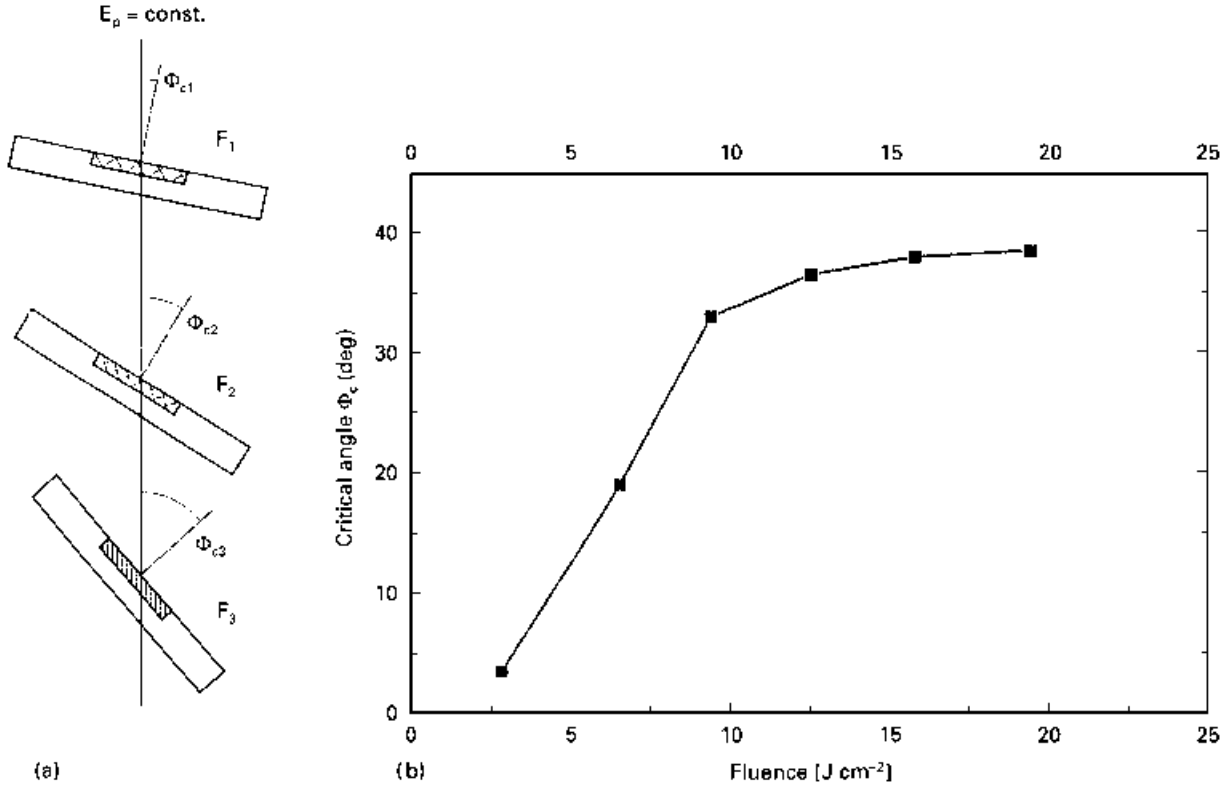

Figure 8 Dependence of the critical angle, Φ_c, of specimen tilting, necessary to neutralize charge-up inside the laser irradiation spot, on the laser fluence, F, for an MAP-treated (111) surface of CaF_2 (a) Schematic drawing showing the dependence of angle Φ_c on increasing fluences, F_1, F_2, F_3. (b) Experimentally measured Φ_c versus F.

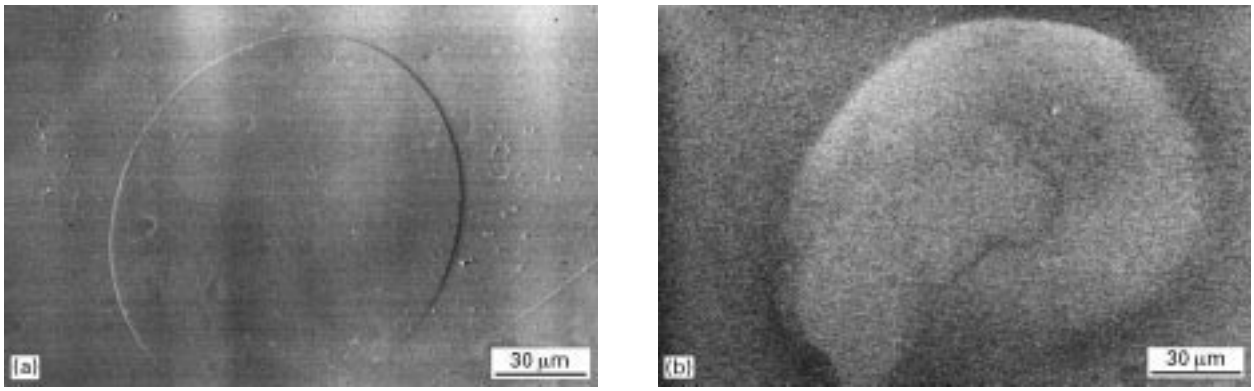

Figure 9 CMP-treated (111) surface of CaF_2 subjected to 248 nm single-shot laser damage at different laser fluences, F. SEM imaging at $E_p = 5$ keV, $\Phi = 45°$. (a) $F = 31.14\,J\,cm^{-2}$, the slow scan mode reveals only a topographic, ring-shaped depression. (b) $F = 29.65\,J\,cm^{-2}$, threshold features only detectable by the TV scan mode.

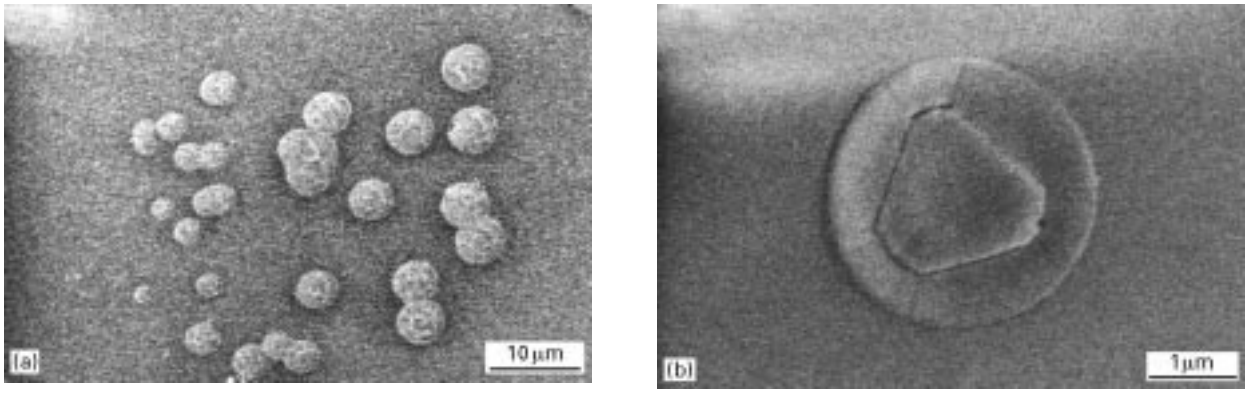

Figure 10 CMP treated (111) CaF_2 surface subjected to laser damage by 193 nm multi shot irradiation. SEM imaging at $E_p = 5$ keV, $\Phi = 29°$, TV scan mode. (a) $F = 13\,J\,cm^{-2}$, 10 shots; (b) $F = 18\,J\,cm^{-2}$, 5 shots.

contrast. A typical result shown in Fig. 11. Crystal defects and defective regions appear by dark contrast. This is strongest near the surface, indicating a high density of defects which decreases more or less monotonically at increasing depth. Below a depth of about 100 nm, individual lines can be resolved which indicate the presence of dislocation loops or fragments of loops as indicated by L in Fig. 11. (It should be noted that dislocations produce sharp lines, while blurred dark lines represent Bragg bending contours which arise from long-range strain fields surrounding the dislocations.) Such individual dislocations were found up to a depth of about 1 μm. At depth of about 200 nm, surface-parallel bright lines, M, are visible which may indicate (1 1 1) microcracks parallel to the surface.

In contrast to MAP, careful CMP is able to remove this defective layer and to avoid dislocations entirely. This is well known from semiconductor and other wafers commercially polished by CMP and investigated by cross-sectional high-resolution TEM of, for example, epitaxial film systems. Such micrographs – taken by us for various semiconductors and oxide crystals – show that the lattice of the substrate wafer is undisturbed up to its epitaxial surface [25].

4.5. Chemical deep etching

Deep etching with 0.2 N HNO_3 was performed in order to reveal defects and to compare the MAP and CMP treatments by this additional method, as shown in Fig. 12. While the MAP surface exhibits a strong roughness after etching (Fig. 12a), the CMP surface appears more perfect after deep etching. Its topography (Fig. 12b) shows features due to etching of scratches, but the topographic contrast is much reduced in spite of a larger surface tilt used to enhance this contrast.

On the other hand, if perfectly CMP-treated surfaces of dielectrics are deep etched, they do not appear to be degraded, and only rare defects of the as-grown type become visible [21].

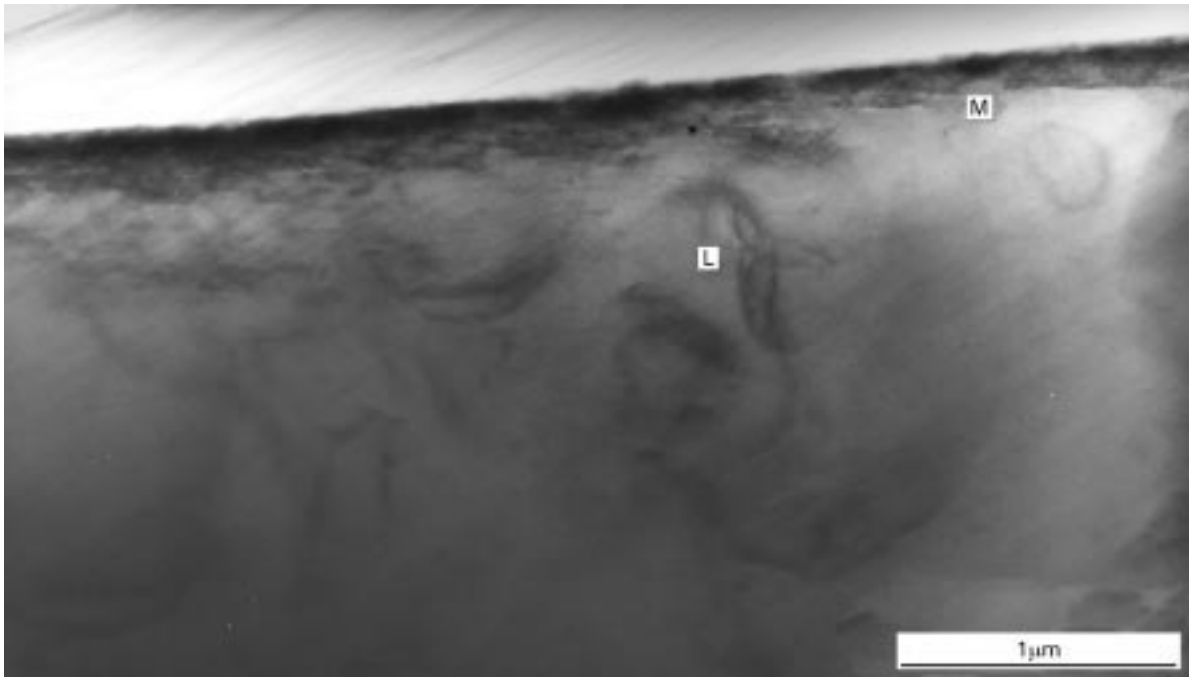

Figure 11 Cross-sectional TEM at an MAP-treated (111) CaF_2 crystal surface showing dark contrast of crystal defects and of strain fields around dislocations, L, and possible microcracks at M.

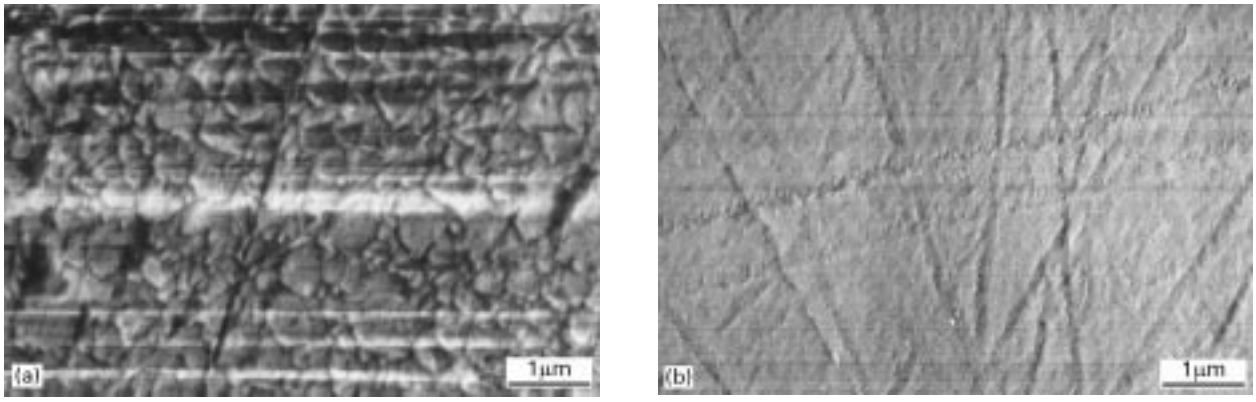

Figure 12 Chemically deep etched (111) CaF_2 crystal surface, SEM imaged at $E_p = 5$ keV after different polishing: (a) MAP, $\Phi = 20°$; (b) two-step incomplete CMP after MAP, $\Phi = 45°$.

5. Discussion

5.1. Effect of polishing on the charge-up and charge decay in the SEM

The enhanced density of defects of MAP-treated ionic crystals directly correlates with the energetic localization of surface charges: in the perfect insulator the injected carriers are localized in the valence or conduction band and neutralized at the external contacts. However, in many real insulators, electrons are additionally localized on defects. Probably, the defects generated by MAP dominate the charging behaviour. These MAP-induced defects are considered to be extrinsic, in addition to those extrinsic defects [26] already present.

Therefore, SE yield measurements cannot simply be correlated with the surface topography or the chemical composition. As found from samples of different sources, the SE yield characteristics are essentially influenced by pretreatments, e.g. thermal history, precleaning, or irradiation treatments.

It is difficult to measure the surface charge storage of insulators because the injected carriers (electrons) interact with the material by complicated trapping processes [17, 39]. Neither the SEM observation of charge-up nor of the local charge decay allows one to decide which of the following factors has the strongest influence on the actual *surface* conductivity: the number of charge carriers, their mobility, or the combination of both. In addition to these given properties, the electrical conductivity is affected by the scanning electron beam. Additionally, excess carriers from *outside* the scanned area can move into this region. Therefore, time-dependent SE yield variations only represent a charge balance resulting from the interaction of these processes.

However, the polarity of the charge-up in the SEM can be uniquely stated for both MAP- and CMP-treated (1 1 1) surfaces of CaF_2. In the case of MAP and an orthogonal beam incidence, the surface is sufficiently free of charge at $E_p = 1.8\,\mathrm{keV}$. This energy is known as E_2 of CaF_2 [19]. A slightly larger $E_p = 2\,\mathrm{keV}$ as in Fig. 1b results in very weak negative charge-up, as expected. Consequently, tilting to $\Phi = 32^\circ$ leads to positive charge-up as in Fig. 1a where $E_2 = 2.4\,\mathrm{keV}$ is known for CaF_2 [19] at this angle of electron incidence. By measuring the "Duane–Hunt high energy cut-off" of the emitted Bremsstrahlung by X-ray energy dispersive spectroscopy (EDS) [40], the true surface potential in the range of $1.5\,\mathrm{keV} < E_p < 8\,\mathrm{keV}$ has been shown to decrease not more than by $\approx 10\%$ versus E_p for CaF_2 [36]. In general, the positive, zero, or negative charge-up of CaF_2 can be adjusted independently by both E_p and Φ within defined limits. In the case of MAP, the observed narrow transition region of $\Delta\Phi = 2^\circ$ results from the very small emission depth of SE (maximum $\approx 50\,\mathrm{nm}$ in insulators [41]) compared with the depth of the subsurface damage layer of several 100 nm. In contrast to this, the drastic increase of $\Delta\Phi$ after the CMP treatment indicates the removal of this damage layer. Therefore, the SEM characterization by determining the charge-up and its transition region, $\Delta\Phi$, offers a sensitive method for characterizing the surface properties of the insulator.

To study the charge leakage behaviour in the SEM, a conducting mesh of uniform contact with the surface is required, and low-voltage imaging in the range $E_p < E_2$ is most convenient because then $\delta \approx \delta_{max}$ is easy to achieve. In case of MAP surfaces, the decay occurred non-exponentially with time. Therefore, one can assume the intrinsic carrier density is small in contrast to the beam-injected charge density. The decay always starts in the centre of the meshes but not homogeneously for all of them. The dominant inhomogeneity is a gradient from the aluminium bar towards the free surface inside the mesh. The peripheral zone of every mesh can be regarded as a retarding field zone. In this zone the uncoated insulator surface can be studied sufficiently free of charge for $E_p > E_2$ [42]. The contrast reversal of the aluminium grid (Fig. 6b–e) takes place gradually during the discharging process. This points to the fact that the nature of the aluminium cross-grid contact to ground is constant but non-ohmic.

In contrast to this, the charge decay of CMP surfaces happens very quickly. Also, at higher magnification, no local variations of charge-up during multiple frame scans were detected.

5.2. SEM detection of the laser damage threshold

On MAP-treated CaF_2 the dependence of charge-up on Φ holds for the non-irradiated crystal surface as well as for the laser-irradiated area. However, the charge-up behaviour within laser spots above the damage threshold II (charge-up) and below the damage threshold III (first oriented cracks) can be treated as that of "insulating islands" of increased permittivity with respect to its surrounding. It is known that there is an inverse relation between the permittivity and the band gap of dielectrics [43]. As mentioned above, MAP increases the density of localized levels within the band gap. Hence it is supposed that MAP reduces the band gap, thus increasing the permittivity. In a similar way, laser irradiation should first affect the localized level, thus leading to changes in the permittivity and of the changing behaviour. This may also be valid for the CMP laser damage threshold: slowly increasing SE yield (Fig. 10b) possibly indicates early stages of local capacitor formation (by the beginning surface exfoliation) which is only detectable by SEM, if very short dwell times of the electron probe in the TV scan mode are used.

6. Conclusion

A change in local surface properties of dielectrics has been sensitively characaterized by studying the electron beam-induced charge-up and discharge behaviour during SEM imaging. The behaviour of mechanical-abrasive polished (MAP-treated) (1 1 1) surfaces of CaF_2 can be interpreted to arise from locally trapped charges if the dielectric surface, dominated by localized state, show an effectively reduced band gap and hence increased dielectric constant. This conclusion is supported by the fact that the charge-up and charge decay processes typical of MAP disappear

if the surfaces are treated by chemomechanical polishing (CMP). Therefore, chemomechanical polishing is assumed to decrease considerably the density of near-surface states.

From the methodical point of view, the charge decay characteristics observed by SEM provide information on the ratio of the injected to intrinsic carrier density of a dielectric surface.

The charge-up and charge decay SEM methods used here advantageously complement X-ray diffraction studies performed during successive surface stripping of MAP dielectrics [22], electrometer probe techniques, and pulsed electroacoustic methods for measuring the charge accumulation in solid dielectrics [44]. It would be particularly advantageous to apply all methods after successive finishing steps of one specific surface as well as after the final state of different finishing techniques.

We found that CMP of (1 1 1) CaF_2 surfaces guarantees a significant enhancement of the ultraviolet laser damage threshold up to 12-fold, in comparison to MAP in the range $1\,J\,cm^{-2} < F < 40\,J\,cm^{-2}$. The SEM methods used here are able to characterize laser damage not only by imaging topographic features, such as depression and the known photoablation (cracking and chipping) processes. Moreover, SEM studies of charge up and charge decay are able to detect very early stages of damage that give rise to changes in the SE yield. Probably, this early damage is determined by photochemical decomposition [45] as the dominant energy deposition. Therefore, the SE yield should be sensitive to the accumulation of surface defects during multiple laser irradiation too.

Acknowledgements

The authors are indebted to Professor E. Matthias, Physics Department, Freie Universität Berlin, for detailed discussions, G. Herbst, Laser Laboratory Berlin-Adlershof, for carrying out laser irradiations at 193 nm, and Professor U. Gösele, Max Planck Institute of Microstructure Physics, for providing experimental and room facilities.

References

1. M. NEGISHI, A. DEGUCHI, M. ANDO, M. TAKIMOTO and N. NAKAMURA, *Nanotechnology* **6** (1995) 139.
2. T. W. WALKER, A. H. GUENTHER and P. E. NIELSEN, *IEEE J. Quantum Electr.* **QE-17** (1981) 2053.
3. R. BOLAND, J. NEWCOMB and A. TURNER, *Proc. SPIE Int. Soc. Opt. Eng.* **2536** (1995) 288.
4. H.-J. HEIMBECK, *Opt. Eng.* **34** (1995) 2719.
5. T. KASAI, K. HORIO, T. YAMAZAKI, M. KOMODA, T. K. DOY and N. KUBO, *J. Non-Cryst. Solids* **177** (1994) 397.
6. S. ROTTER, U. LACHISH and U. EL-HANANY, *J. Cryst. Growth* **73** (1985) 187.
7. G. J. PIETSCH, Y. J. CHABAL and G. S. HIGASHI, *J. Appl. Phys.* **78** (1995) 1650.
8. R. R. TURK, J. A. HARRINGTON, J. JOHNSTON, C. HAEUSSLER and R. L. JOYCE, *Appl. Optics* **18** (1979) 957.
9. J. W. DAVISSON, *J. Mater. Sci.* **9** (1974) 1701.
10. R. JAIRATH, J. FARKAS, C. K. HUANG, M. STELL and S.-M. TZENG, *Solid State Technol.* **34** (7) (1994) 71.
11. J. HAISMA, B. A. C. M. SPIERINGS, U. K. P. BIERMAN and A. A. VAN GORKUM, *Appl. Optics* **33** (1994) 1154.
12. G. RINGEL, F. KRATZ, D.-R. SCHMITT, J. MANGELSDORF, F. CREUZER and J. GARRATT, *Proc. SPIE Int. Soc. Opt. Eng.* **2536** (1995) 317.
13. Y. ZHENG, *ibid.* **2544** (1995) 157.
14. W. GUTMANNSBAUER, H. J. HUG and E. MEYER, *Microelectron. Eng.* **32** (1996) 389.
15. D.-R. SCHMITT, *Precis. Eng.* **13** (1990) 203.
16. P. D. WARREN, C. PECORARI, O. V. KOLOSOV, S. G. ROBERTS and G. A. D. BRIGGS, *Nanotechnology* **7** (1996) 295.
17. R. G. BOMMAKANTI and T. S. SUDARSHAN, *J. Appl. Phys.* **67** (1990) 6991.
18. T. ICHINOKAWA, M. IIYAMA, A. ONOGUCHI and T. KOBAYASHI, *Jpn. J. Appl. Phys.* **13** (1974) 1272.
19. L. REIMER, U. GOLLA, R. BÖNGELER, M. KÄSSENS, B. SCHINDLER and R. SENKEL, *Optik* **92** (1992) 14.
20. G. F. VANDER VOORT, *Z. Materialogr.* **2** (1992) 3.
21. S. LAFFEY, M. HENDRICKSON and J. R. VIG, in Proceedings of the 16th Piezoelectric Device Conference", Vol. 1, Kansas City, Sept 1994 (Electron Industries Association, Washington DC, 1994) p. 95.
22. B. DIETRICH, E. FÖRSTER and R. BÖTTGER, *Kristall Technik* **12** (1977) 609.
23. R. A. SCHWARZER, *Mater. Sci. Forum* **157/162** (1992) 187.
24. K. E. PUTTICK, L. C. WHITMORE, C. L. CHAO and A. E. GEE, *Philos. Mag. A* **69** (1994) 91.
25. G. KÄSTNER, D. HESSE, R. SCHOLZ, H. KOCH, F. LUDWIG, M. LORENZ and H. KITTEL, *Physica C* **243** (1995) 281.
26. R. C. ALIG and S. BLOOM, *J. Appl. Phys.* **49** (1978) 3476.
27. J. P. GANACHAUD and A. MOKRANI, *Surf. Sci.* **334** (1995) 329.
28. Y. ISHIBASHI, T. KODAMA, H. OIWA and Y. UCHIKAWA, *Scanning* **14** (1992) 219.
29. J. CAZAUX, K. H. KIM, O. JBARA and G. SALACE, *J. Appl. Phys.* **70** (1991) 960.
30. R. D. VAN VELD and T. J. SHAFFNER, in "Proceedings of the 4th Annual Scanning Electron Microscope Symposium", Part I, edited by Om Johari and Irene Corvin (ITT Research Institute, Chicago, IL, 1971) p. 17.
31. V. T. JORDANOV and G. F. KNOLL, *IEEE Trans. Nucl. Sci.* **42** (1995) 683.
32. H. RICKERT, *Angew. Chem.* **90** (1978) 38.
33. R. W. FATHAUER and L. J. SCHOWALTER, *Appl. Phys. Lett.* **45** (1984) 519.
34. B. GROSS and L. N. DE OLIVEIRA, *J. Appl. Phys.* **45** (1974) 4724.
35. H.-J. FITTING, *Phys. Status Solidi* (*a*) **26** (1974) 525.
36. H. JOHANSEN, S. GOGOLL, E. STENZEL, M. REICHLING and E. MATTHIAS, *Scanning* **19** (1997) 416.
37. R. L. WEBB, L. C. JENSEN, S. C. LANGFORD and J. T. DICKINSON, *J. Appl. Phys.* **74** (1993) 2323.
38. S. GOGOLL, E. STENZEL, H. JOHANSEN, M. REICHLING and E. MATTHIAS, *Nucl. Instrum. Meth. Phys. Res.* **B 116** (1996) 279.
39. J. P. VIGOUROUX, J. P. DURAUD, A. LE MOEL, C. LE GRESSUS and D. L. GRISCOM, *J. Appl. Phys.* **57** (1985) 5139.
40. K. F. J. HEINRICH, "Electron Beam X-Ray Microanalysis" (Van Nostrand Reinhold, New York, NY, 1981).
41. H. SEILER, *Z. Angew. Phys.* **22** (1967) 249.
42. H. JOHANSEN, S. GOGOLL, E. STENZEL and M. REICHLING, *Phys. Status Solidi* (*a*) **150** (1995) 613.
43. T. S. SUDARSHAN and J. WANG, *IEEE Trans. Electr. Insul.* **27** (1992) 1127.
44. E. D. PALIK, J. W. GIBSON and R. T. HOLM, *Surface Sci.* **84** (1979) 164.
45. Y. LI, M. YASUDA and T. TAKADA, *IEEE Trans. Dielectr. Insul.* **1** (1994) 188.

Received 14 October 1997
and accepted 15 May 1998